Ratio of orbital-to-spin magnetic moment in Co core-shell nanoparticles

U. Wiedwald, M. Spasova, E. L. Salabas, M. Ulmeanu, and M. Farle
Institut für Physik, Universität Duisburg-Essen, Lotharstrasse 1, 47048 Duisburg, Germany

Z. Frait
Institute of Physics, Academy of Science of the Czech Republic, Na Slovance, 18221 Prague 8, Czech Republic

A. Fraile Rodriguez and D. Arvanitis
Department of Physics, Uppsala University, Box 530, 75121 Uppsala, Sweden

N. S. Sobal, M. Hilgendorff, and M. Giersig
Caesar Research Center, Department of Nanoparticle Technology, Ludwig-Erhard-Allee 2, 53175 Bonn, Germany

Arrays of monodisperse colloidal 11.4-nm Co nanoparticles were investigated by multifrequency ferromagnetic resonance and x-ray magnetic circular dichroism (XMCD). The ratio of orbital-to-spin magnetic moment $\mu_L/\mu_S^{\mathrm{eff}}=0.24\pm0.06$ determined by XMCD is 300% enhanced in comparison to the ratio obtained from a g-factor analysis which yields $g=2.150\pm0.015$ corresponding to $\mu_L/\mu_S^{\mathrm{eff}}=0.075\pm0.008$ (bulk fcc Co $\mu_L/\mu_S^{\mathrm{eff}}=0.08$). We show that the difference can be explained by the presence of uncompensated Co magnetic moments at the interface to a 2–2.5-nm CoO shell surrounding a metallic fcc-like Co core. This magnetic analysis is confirmed by high-resolution transmission electron microscopy.

Magnetic nanoscale particles (MNPs) with a narrow size distribution and diameters in the range of 4 to 15 nm have attracted much experimental effort recently (see, e.g., Refs. 1–6). Wet-chemical synthesis methods yield magnetic spherical nanoparticles in large quantities with a controlled composition and diameter, with a narrow size distribution and with ultrahigh purity. Colloidal magnetic particles, such as FePt or Co, covered with a ligand shell of long-chain hydrocarbons, for example, have been studied extensively by many groups.[7–10] The ligand shell of organic materials around the particles has been considered to act as a protective shell against the oxidation of the metallic core.

In MNPs the interaction of the orbital (μ_L) and spin (μ_S) parts of the total magnetic moment ($\mu_t=\mu_S+\mu_L$) becomes important due to the unquenching of the orbital magnetic moment at the surface and in noncubic crystal structures. The surface contribution becomes especially important in MNPs. For example, 50% of all atoms in a sample consisting of nanoparticles of 3-nm diameter are surface atoms. Furthermore, due to this large ratio of surface-to-volume atoms the effective magnetic anisotropy energy density (K_{eff}) is strongly influenced by the surface conditions.

Ferromagnetic resonance (FMR), paramagnetic resonance (EPR), and x-ray magnetic circular dichroism (XMCD) are the methods of choice to study the effects of orbital magnetism in monodisperse nanoparticles with different depth resolutions. Combining EPR/FMR which has a sampling depth of several tens of nanometers at resonance—thus measuring all of the nanoparticle—and XMCD which has a sampling depth of 2 to 3 nm in total electron yield mode allows the investigation of shell and core magnetism in 10–15-nm-diameter particles. In $3d$ elements the spectroscopic g factor[11] which is measured by EPR/FMR is proportional to the ratio of the orbital-to-spin magnetic moment μ_L/μ_S. In

XMCD the temperature-independent ratio can be determined using magneto-optical sum rules.[12] Usually the determination of the g factor based on FMR measurements is very complicated due to large intrinsic magnetic anisotropy fields which are temperature dependent.[13–15] In ensembles of superparamagnetic nanoparticles above their blocking temperature, however, the intrinsic magnetic fields become negligibly small due to thermal fluctuations. A straightforward g factor analysis in terms of the paramagnetic resonance condition becomes possible.

In the following we present structural and magnetic results on highly monodisperse colloidal Co nanoparticles with 11.4-nm diameter and a size deviation of less than 5%. It is demonstrated by high-resolution transmission electron microscopy (HR-TEM) that the nominally metallic particles consist of an fcc-like metallic core with a thin passivating fcc CoO layer embedded in a hydrocarbon corona. Using the complimentary techniques of FMR/EPR and XMCD we find a large enhancement of orbital magnetic moment at the strained interface between the antiferromagnetic CoO shell (2–2.5 nm) and the metallic ferromagnetic Co core (7–8 nm). Despite the large mismatch at the interface the core shows a fcc structure with a bulklike ratio of orbital-to-spin magnetic moment.

Highly monodisperse Co MNPs were prepared by the thermal decomposition of dicobaltoctacarbonyl $[\mathrm{Co_2(CO)_8}]$ in toluene as described previously.[16,17] A concentrated toluene-based Co nanoparticle solution remains chemically and magnetically stable for at least one year when stored in an oxygen-free atmosphere. For all magnetic and structural investigations the arrays of particles were dried on flat substrates (FMR: Si, XMCD: Mo, TEM: carbon-coated Cu grid). The different substrates for the different techniques were chosen for technical reasons and had no influence on

the results discussed below. The crystallographic structure and chemical composition of individual Co MNPs were determined by HR-TEM, selected area electron diffraction (SAED), and electron energy-loss spectroscopy (EELS).[18] The magnetic properties of the arrays of Co MNPs were characterized by superconducting quantum interference device (SQUID) magnetometry, FMR, and XMCD. FMR was measured at three frequencies of 9.8, 35.7, and 69.7 GHz at room temperature. For all microwave frequencies absorption spectra were recorded with the external magnetic field applied in the film plane and normal to the film plane. X-ray-absorption spectroscopy (XAS) and XMCD of arrays of Co MNPs at the Co $L_{2,3}$ edges were measured at beam line D1011 at the MAX-Laboratory synchrotron facility in Lund, Sweden. The XAS spectra were taken with linear polarized light in the total electron yield mode at normal incidence. Circular polarized light spectra for XMCD were recorded in remanence at an angle of 20° with respect to the substrate plane. Angular-dependent spectra (20°–90°) were recorded, confirming the in-plane easy axis of magnetization. No perpendicular magnetic component was found. The magnetization was reversed by pulses of 50 mT applied in the film plane. All spectra were normalized by an I_0 signal taken with a gold grid. We deduced the ratio of orbital-to-spin magnetic moment by a standard procedure employing the sum rules as described elsewhere.[12,19] For the XAS and XMCD investigations the Co colloidal solution was dried *ex situ* onto a clean, polished Mo foil. The concentration was chosen to achieve a coverage of several monolayers of MNPs. The spectra were recorded under ultrahigh vacuum conditions (base pressure $<5 \times 10^{-7}$ Pa) between 20 K and 300 K. Core-level spectroscopies were performed for the as-prepared state and after a stepwise Ar$^+$-ion etching process to remove the chemical residue due to the magnetorheological deposition. By comparison of TEM images recorded before and after XMCD measurements we find that neither the size nor the shape of the MNPs changes because of the heat treatment during the bakeout ($\sim$450 K) or the irradiation by x rays for several hours.

The effect of ion etching (3 kV, 4 μA, 135 min) is shown in Fig. 1(a). We find that the white line intensity which is a measure of the number of unoccupied d holes[20] decreases continuously up to ion-etching times of 135 min after which no further changes are observed. We note that none of the spectra reveals a pure metallic character as observed in Co thin films, for example. Accordingly, in the XMCD analysis we took into account contributions from transitions of Co in a nonmetallic environment as discussed below.

Figure 1(b) shows a typical result of the 135-min ion-etched Co nanoparticle array at a temperature of $T=170$ K. For temperatures between 100 K and 200 K a well-resolved XMCD signal was observed. Above and below these temperatures no signal was resolved, since either the remanent magnetization vanished or the coercive field was larger than the available external field (50 mT) for reversal. The ratio of the orbital-to-spin magnetic moment $\mu_L/\mu_S^{\mathrm{eff}}$ is determined to be 0.24±0.06, that is, 300% enhanced in comparison to fcc bulk Co ($\mu_L/\mu_S^{\mathrm{eff}}=0.08$). The rather large error bar is caused by the low remanent magnetization M_R of the array
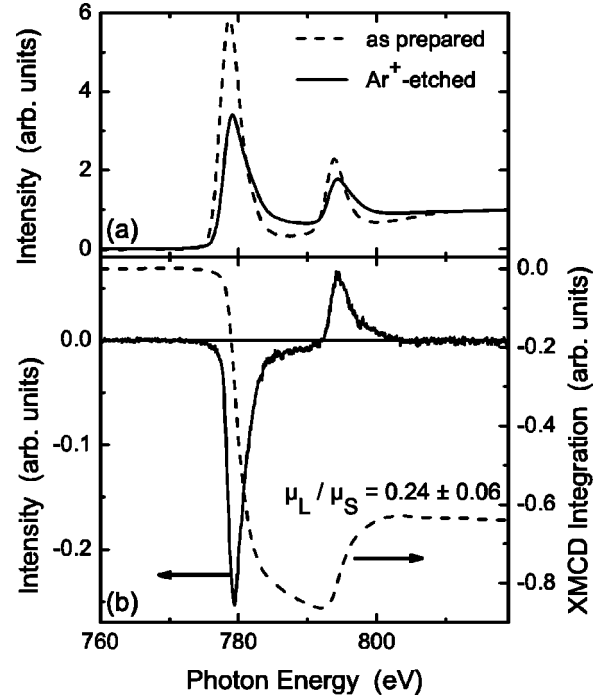

FIG. 1. (a) $L_{3,2}$ XAS of an array of Co MNPs on a Mo substrate before and after Ar$^+$-ion etching (3 kV, 4 μA, 135 min). (b) XMCD difference spectrum (left scale) and its integration (right scale) of an array of Co MNPs taken at $T=170$ K and 20° grazing incidence.

of MNPs and the difficulty in averaging the metallic and nonmetallic contributions. Within the error bar no temperature dependence of $\mu_L/\mu_S^{\mathrm{eff}}$ is found.

Now we turn to the discussion of the results obtained by ferromagnetic resonance. Figure 2(a) shows the FMR spectra recorded at 9.8 GHz, 35.7 GHz, and 69.7 GHz with the external magnetic field applied parallel (pc) and perpendicular (nc) to the sample plane. We always find the lower resonance field $B_{\mathrm{res}\parallel}$ in the (pc) configuration. It is smaller than the paramagnetic resonance field ω/γ, which shows that there is an additional intrinsic magnetic field due to an effective induced magnetization M_{eff} and that the easy axis of M_{eff} is parallel to the sample plane. Using the well-known Kittel FMR equations for the (pc) and (nc) configurations,[15]

$$(\omega/\gamma)^2 = B_{\mathrm{res}\parallel}\{B_{\mathrm{res}\parallel} + 4\pi M_{\mathrm{eff}}(B_{\mathrm{res}\parallel})\}, \qquad (1a)$$

$$(\omega/\gamma) = B_{\mathrm{res}\perp} - 4\pi M_{\mathrm{eff}}(B_{\mathrm{res}\perp}), \qquad (1b)$$

we calculate M_{eff} by an iterative procedure allowing a slight variation of the g factor, $g=\gamma\hbar/\mu_B$, starting from the fcc Co bulk value $g=2.16$. This calculation was done for 35.7 GHz and 69.7 GHz only, and we find $M_{\mathrm{eff}}=67\pm11$ mT. For 9.8 GHz this calculation is more complicated, because M_{eff} is not saturated. It changes during the scan of the magnetic field as confirmed by SQUID magnetometry. This shows up in the spectra at 9.8 GHz [Fig. 2(a)] as a sudden increase of the absorption at low fields. With $M_{\mathrm{eff}}=67\pm11$ mT we calculate the corrected resonance field $B_{\mathrm{res,cor}}$ that does not depend on M_{eff} anymore. For the resonance at 9.8 GHz we had to use the corrected value $M(B_{\mathrm{res}})=0.94M_{\mathrm{eff}}$ which was ob-
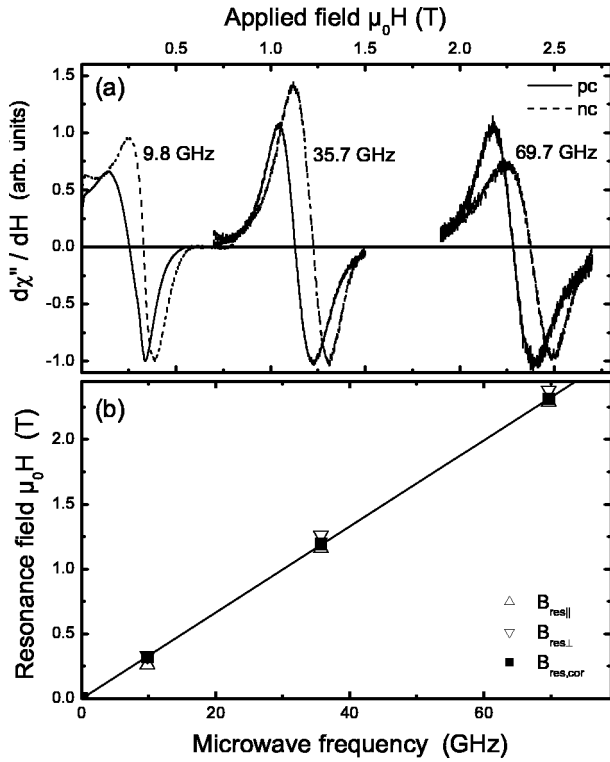
FIG. 2. (a) FMR absorption curves for three different microwave frequencies for pc (solid) and nc (dashed) configurations at room temperature. (b) Experimental resonance fields ($B_{res\parallel}$, $B_{res\perp}$) as a function of the microwave frequency at 300 K. The resonance fields $B_{res,cor}$ corrected for the induced magnetization are also shown (see text). The error bars are smaller than the symbol size.

tained by SQUID magnetometry. The g factor is determined by the paramagnetic-resonance condition $h\nu = g\mu_B B_{res,cor}$. In Fig. 2(b) the experimentally measured resonance fields for the pc and nc configurations ($B_{res\parallel}$, $B_{res\perp}$) and $B_{res,cor}$ are plotted as a function of microwave frequency. A linear fit through the three frequencies and the origin yields a g factor of 2.150 ± 0.015, which is very close to the bulk value of fcc Co ($g=2.16$). The same g factor is obtained in parallel geometry when using the ferromagnetic-resonance condition which yields a quadratic fit[11,14] according to Eq. (1a).

The ratio μ_L/μ_S^{eff} is given by[13] $\mu_L/\mu_S^{eff} = (g-2)/2 = 0.075\pm0.010$, which is bulklike. This result obtained for the same MNPs is in obvious disagreement with the 300% larger ratio measured by XMCD. This apparent contradiction can be resolved by taking into account the different probing depths of the two techniques. FMR measures the collective precession of spins in the entire nanoparticle. The total electron yield mode for XMCD measurements is surface sensitive and detects the signal from Co close to the MNP surface only. For cobalt the electron mean free path is about 2.2 nm, which is the same order of magnitude as the one for CoO (1.9–3.0 nm).[21,22] To explain the large difference in the orbital moment contribution between the XMCD and FMR results one has to assume the presence of the large uncompensated magnetic moment of Co^{2+} ($3d^7$, $6.67\mu_B$, $L=3$, $S=3/2$, $g_J=1.33$) and a large $\mu_L/\mu_S \approx 0.6$.[23] Metallic cobalt is known to form a passivating CoO layer with a typical

thickness of 1–3 nm. We assume in the following that the Co particle is covered by a shell of natural CoO and average the contribution of this shell carrying a large μ_L/μ_S with the contribution from the bulklike metallic core. By taking into account the exponentally decreasing sampling depth of the XMCD signal we find for a CoO shell thickness of $d_{CoO}=2.5$ nm good quantitative agreement to the experimentally measured ratio. Hence, the dichroic signal intensity is attenuated by the CoO shell and the resulting XMCD difference signal has a much stronger contribution from the large interface area of Co/CoO than that from the free metallic fcc Co film. In addition, the presence of the CoO shell was also confirmed by simulating our experimentally measured high-resolution XAS spectra (not shown here) by a superposition of Co and oxidic Co reference spectra.[22] The energy resolution of the spectra shown in Fig. 1(a) is not sufficient for such a curve fitting. However, a rough estimate can be made for the ion-etched sample by neglecting contributions from s-d hybridizations and simulating L edges for metallic Co and CoO by overlapping Gaussian peaks at energies, branching ratios, and the full width at half maximum taken from the literature[24,25] after the subtraction of the step function. By fitting the peak heights, which is the only free parameter, we calculate the contributions from Co and CoO to the total electron yield to be 43% and 57%, respectively. With the electron escape depths $\lambda_{Co}=2.2$ nm and $\lambda_{CoO}=3.0$ nm and the exponential decrease of the XAS sensitivity[22] we find the average thickness of the CoO shell to be 2.5 nm.

Generally, the Co^{2+} in antiferromagnet CoO would not show a XMCD signal. In the core-shell structure of our particles, however, the Co atoms at the Co/CoO interface are disordered and most likely frustrated. Assuming a 2–2.5-nm thick CoO shell and the bulk lattice constant[26] one finds an uneven number of Co ion layers. In this case Co atoms / ions with oxygen binding partners at the Co/CoO interface exhibit uncompensated ("loose") spins. Also the quenching of the orbital moment in a cubic (fcc) CoO crystal is lifted due to the rough and strained interface. The existence of an amorphous phase of CoO cannot be excluded and would also give rise to a strongly enhanced orbital moment.

To confirm the structural and compositional results of the magnetic characterization we performed a high-resolution transmission electron microscopy study in the as-prepared state. We find[27,28] that the particle size distribution follows the log-normal distribution with a most probable diameter of $d_{mp}=11.4$ nm and a standard deviation of $\sigma=1.2$ nm. All particles show a nearly perfect spherical shape. The Co MNPs consist of a metallic Co core, crystallized in the fcc phase. The inner particle structure is multiple twinned parallel to the common {111} plane. The core is encased in an fcc CoO shell. Figure 3 shows TEM images filtered at the Co L_3 edge ($\sim$778 eV) and the oxygen K edge ($\sim$525 eV). The intensity histograms recorded along the same line scan across the nanoparticle show a distribution corresponding to a spherical Co core (7-nm diameter) in Fig. 2(c) covered by a rather uniform oxidic shell [Fig. 2(d)]. Using a Gaussian double peak fitting routine for the simulation of the intensity
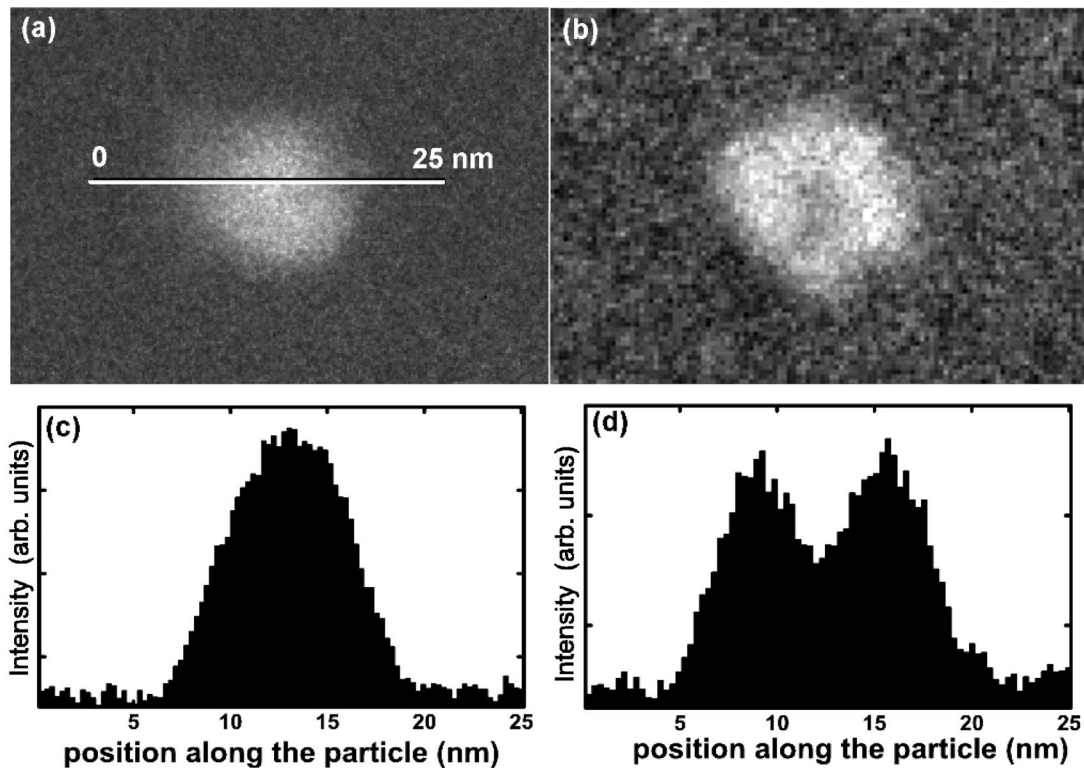
FIG. 3. EELS element-specific mapping of the cobalt (a) and oxygen (b) components in the MNPs. Energy-filtered images are recorded at the Co L_3 edge ($\sim$778 eV) and at the oxygen K edge ($\sim$525 eV). Intensity profiles across the particle show the distribution of cobalt (c) and oxygen (d).

histogram in Fig. 2(d) the thickness of the fcc CoO shell is determined to be 2–2.5 nm, and the diameter of the fcc Co core is 7–8 nm.

Finally, one has to discuss why the contribution of CoO is not observed in FMR. The antiferromagnetic-resonance frequency of the CoO lies at much higher frequencies and cannot be detected with our setup. The contribution of the uncompensated moments at the Co/CoO interface could be described in terms of a ferrimagnetic resonance.[29] However, a simple estimate of the oxidic interface contribution in relation to the metallic Co core shows that one cannot expect to observe a shift of the resonance field outside our given error bar.

In summary, we find that the ratio of orbital-to-spin magnetic moment in 11.4-nm Co MNPs is bulk-like. An apparent enhancement of 300% detected by XMCD is shown to be the result of a thin oxidic interface region. Such types of studies on core-shell structures with their high interface-to-volume atom ratio may offer an interesting experimental approach to the understanding of the correlation of interface orbital magnetism and exchange bias effects in ferromagnetic/antiferromagnetic systems.

[1] R. H. Kodama, J. Magn. Magn. Mater. **200**, 359 (1999).

[2] Y. Qiang, R. F. Sabiryanov, S. S. Jaswal, Y. Liu, H. Haberland, and D. J. Sellmyer, Phys. Rev. B **66**, 064404 (2002).

[3] J. Rockenberger, F. Nolting, J. Luning, J. Hu, and A. P. Alivisatos, J. Chem. Phys. **116**, 6322 (2002).

[4] D. L. Peng, K. Sumiyama, T. Hihara, S. Yamamuro, and T. J. Konno, Phys. Rev. B **61**, 3103 (2000).

[5] H. A. Dürr, S. S. Dhesi, E. Dudzik, D. Knabben, G. van der Laan, J. B. Goedkoop, and F. U. Hillebrecht, Phys. Rev. B **59**, R701 (1999).

[6] C. T. Black, C. B. Murray, R. L. Sandstrom, and Shouheng Sun, Science **290**, 1131 (2000).

[7] C. B. Murray, Shouheng Sun, W. Gaschler, H. Doyle, T. A. Betley, and C. R. Kagan, IBM J. Res. Dev. **45**, 47 (2001).

[8] V. Russier, C. Petit, J. Legrand, and M. P. Pileni, Phys. Rev. B **62**, 3910 (2000).

[9] V. F. Puntes, K. M. Krishnan, and P. Alivisatos, Appl. Phys. Lett. **78**, 2187 (2001).

[10] Shouheng Sun, C. B. Murray, D. Weller, L. Folks, and A. Moser, Science **287**, 1989 (2000).

[11] A. N. Anisimov, M. Farle, P. Poulopoulos, W. Platow, K. Baberschke, P. Isberg, R. Wappling, A. M. N. Niklasson, and O. Eriksson, Phys. Rev. Lett. **82**, 2390 (1999).

[12] J. Stöhr, J. Magn. Magn. Mater. **200**, 470 (1999).

[13] C. Kittel, J. Phys. Radiat. **12**, 291 (1951).

[14] J. Pelzl, R. Meckenstock, D. Spoddig, F. Schreiber, J. Pflaum, and Z. Frait, J. Phys.: Condens. Matter **15**, S451 (2003).

[15] M. Farle, Rep. Prog. Phys. **61**, 755 (1998).

[16] J. S. Yin and Z. L. Wang, Phys. Rev. Lett. **79**, 2570 (1997).

[17] M. Giersig and M. Hilgendorff, J. Phys. D **32**, L111 (1999).

[18] For standard TEM and SAED a Philips CM12 and a JEOL 3010 microscope were used, while high-resolution TEM pictures were taken with the Berkeley Atomic Resolution Microscope with an acceleration voltage of 800 kV. Microchemical analysis was conducted with a Philips CM200 field-emission microscope with a probe size of 0.8 nm, using an imaging energy filter and an energy dispersive x-ray analyzer.

[19] D. Arvanitis, M. Tischer, J. Hunter Dunn, F. May, N. Martensson, and K. Baberschke, *Lecture Notes in Physics*, edited by H. Ebert and G. Schütz (Springer-Verlag, Berlin, 1996), Vol. 466.

[20] M. Tischer, O. Hjortstam, D. Arvanitis, J. Hunter Dunn, F. May, K. Baberschke, J. Trygg, J. M. Wills, B. Johansson, and O. Eriksson, Phys. Rev. Lett. **75**, 1602 (1995).

[21] H.-G. Boyen, G. Kästle, K. Zürn, T. Herzog, F. Weigl, P. Ziemann, O. Mayer, C. Jerome, M. Möller, J. P. Spatz, M. G. Garnier, and P. Oelhafen, Adv. Funct. Mater. **13**, 359 (2003).

[22] T. J. Regan, H. Ohldag, C. Stamm, F. Nolting, J. Lüning, J. Stöhr, and R. L. White, Phys. Rev. B **64**, 214422 (2001).

[23] G. Ghiringhelli, L. H. Tjeng, A. Tanaka, O. Tjernberg, T. Mizokawa, J. L. de Boer, and N. B. Brookes, Phys. Rev. B **66**, 075101 (2002).

[24] C. D. Wagner, W. M. Riggs, L. E. Davis, J. F. Moulder, and G. E. Muilenberg, *Handbook of X-ray Photoelectron Spectrocopy*, edited by C. D. Wagner (Perkin-Elmer, Eden Prairie, Minnesota, 1979).

[25] C. D. Wagner, A. V. Naumkin, A. Kraut-Vass, J. W. Allison, C. J. Powell, and J. R. Rumble, Jr., *NIST X-ray Photoelectron Spectroscopy Database* (NIST, Gaithersburg, MD, 2003); http://srdata.nist.gov/xps

[26] W. Jauch and M. Reehuis, Phys. Rev. B **65**, 125111 (2002).

[27] M. Spasova, T. Radetic, N. S. Sobal, M. Hilgendorff, U. Wiedwald, M. Farle, M. Giersig, and U. Dahmen, Mater. Res. Soc. Symp. Proc. **721**, 195 (2002).

[28] M. Spasova, U. Wiedwald, R. Ramchal, M. Farle, M. Hilgendorff, and M. Giersig, J. Magn. Magn. Mater. **240**, 40 (2002).

[29] M. Farle, A. N. Anisimov, K. Baberschke, J. Langer, and H. Maletta, Europhys. Lett. **49**, 658 (2000).